JOURNAL OF PROPULSION AND POWER
Vol. 21, No. 1, January–February 2005

Influence of Shock Wave on Turbomachinery Blade Row Flutter

R. Srivastava* and T. G. Keith Jr.†
University of Toledo, Toledo, Ohio 43606

The influence and effect of a shock wave on the flutter characteristics of a turbomachinery blade row is described. High-fidelity numerical analysis is used to understand the behavior of turbomachinery blade row flutter in the presence of an oscillating shock wave. The unsteady Navier–Stokes equations are solved on a dynamically deforming, body-fitted grid to obtain the unsteady aerodynamic load on a vibrating blade. An energy exchange method is used for calculating the aerodynamic damping to determine the blade row flutter characteristics. A transonic forward swept fan configuration, which showed flutter at part speed conditions in wind-tunnel tests, is analyzed. The shock wave was found to influence strongly the aerodynamic damping, with outboard stations providing the main contribution. The interblade phase angle of blade motion and the location of shock wave determined the influence of shock wave on blade stability. The influence of shock motion was found to be linear for a small amplitude of blade oscillation. The observations from the numerical analysis are used to develop an algebraic model for calculating the work done on the blade because of an oscillating shock wave.

Introduction

FLUTTER in turbomachinery blade rows is a significant design concern. Modern fans, being designed to reduce noise, are swept forward, have thin blade cross sections, and lean in the plane of rotation. These features coupled with transonic flow result in aeroelastic problems, requiring a three-dimensional viscous analysis to calculate accurately the flutter characteristics. Shock waves strongly influence the flutter characteristics of blade rows. The shock waves could have a stabilizing or destabilizing effect on blade stability. It is important for a designer to know how various geometric and flow features impact the shock impulse-induced aeroelastic characteristic of the blade row.

Several methods have been developed for the prediction of aeroelastic characteristics with various degrees of fidelity. For turbomachinery blade rows, flutter is observed primarily in a single natural mode, with oscillating shock waves on the blade surfaces being one of the primary sources for instability. Single-mode flutter can be captured using the energy exchange method. Aeroelastic analyses based on the energy exchange between vibrating blades and the surrounding fluid have been reported for turbomachines by the use of semi-analytical methods,[1,2] the linearized Euler method (see Ref. 3), Euler methods (see Refs. 4–6), the linearized viscous method,[7] and viscous methods.[8–10] A limited number of coupled aeroelastic analyses of turbomachine configurations have also been reported.[11–13] Williams et al.[11] used a linear panel method to solve the eigenvalue problem. Gerolymos[12] and Srivastava and Reddy[13] solved the coupled aeroelastic equations based on an inviscid aerodynamic analysis.

Recent analyses of turbomachinery blade row flutter[14–18] have indicated the flutter to be strongly influenced by shock and its characteristics. Panovsky et al.,[14] using the three-dimensional viscous aeroelastic analysis code TURBO-AE,[6] reported good correlation with observed wind-tunnel flutter near the stall line for an experimental forward swept fan.[19] Srivastava et al.[15] found that the flutter observed in Ref. 19 was driven primarily by a shock on the suction surface and that the shock location and strength strongly influenced the flutter characteristics. Sanders et al.[16] reported good correlation of stall-side flutter using the TURBO-AE code with measurements and concluded that the code successfully captures the relevant flow physics. These studies showed that, although the high-angle-of-attack flutter occurred near the stall line, the flutter characteristics were driven primarily by the shock and its characteristics rather than by flow separation. Some preliminary analysis carried out by the authors has shown that, although flow separation may exist near the stall line, it contributes little toward the energy exchange. The flow separation, however, influences the mass flow, dictating the location and strength of the shock. Calculations reported by Isomura and Giles[18] for flutter instability near the stall line in a transonic fan also showed that unsteady shock oscillations rather than blade stall were the driving mechanism for flutter.

The objective of the present study is to better understand the impact and influence of shock waves on the flutter characteristics of a turbomachinery blade row, to develop simple models that incorporate sufficient physics to allow for rapid flutter calculations. The energy exchange method, based on a three-dimensional viscous unsteady aerodynamic code reported in Ref. 6, is used here to study the observed flutter in a greater detail. Several studies using the Navier–Stokes flutter analysis code TURBO-AE are conducted to better understand the influence of shock wave on flutter behavior and its relation to various parameters.

Aerodynamic Analysis

The aeroelastic analysis code TURBO-AE reported in Ref. 6 is based on the aerodynamic code TURBO.[20,21] TURBO solves the unsteady three-dimensional Navier–Stokes equations for the internal flows of axial flow turbomachinery components. The solver can model multiple blade rows undergoing harmonic oscillations with arbitrary interblade phase angles (IBPAs). Good comparisons with experimental data for steady and unsteady aerodynamic analyses have been reported using the TURBO code.[22,23] A brief description of the solution method is provided here.

The Navier–Stokes equation in conservation form can be written as

$$\frac{\partial \boldsymbol{q}}{\partial t} + \frac{\partial (\boldsymbol{E} - \boldsymbol{E}_v)}{\partial x} + \frac{\partial (\boldsymbol{F} - \boldsymbol{F}_v)}{\partial y} + \frac{\partial (\boldsymbol{G} - \boldsymbol{G}_v)}{\partial z} = 0 \qquad (1)$$

where $\boldsymbol{q}$ is the vector of unknown flow variables in conservation form

$$\boldsymbol{q} = \begin{Bmatrix} \rho \\ \rho u \\ \rho v \\ \rho w \\ e \end{Bmatrix}$$

Received 22 September 2003; revision received 9 April 2004; accepted for publication 9 April 2004.

*Senior Research Associate, Department of Mechanical, Industrial, and Manufacturing Engineering. Senior Member AIAA.

†Distinguished University Professor, Department of Mechanical, Industrial, and Manufacturing Engineering. Associate Fellow AIAA.

with

$$\boldsymbol{E} = \begin{Bmatrix} \rho u \\ \rho u^2 + p \\ \rho uv \\ \rho uw \\ u(e+p) \end{Bmatrix}, \qquad \boldsymbol{F} = \begin{Bmatrix} \rho v \\ \rho uv \\ \rho v^2 + p \\ \rho vw \\ v(e+p) \end{Bmatrix}$$

$$\boldsymbol{G} = \begin{Bmatrix} \rho w \\ \rho uw \\ \rho wv \\ \rho w^2 + p \\ w(e+p) \end{Bmatrix}, \qquad \boldsymbol{E}_v = \begin{Bmatrix} 0 \\ \tau_{xx} \\ \tau_{xy} \\ \tau_{xz} \\ Q_x \end{Bmatrix}$$

$$\boldsymbol{F}_v = \begin{Bmatrix} 0 \\ \tau_{yx} \\ \tau_{yy} \\ \tau_{yz} \\ Q_y \end{Bmatrix}, \qquad \boldsymbol{G}_v = \begin{Bmatrix} 0 \\ \tau_{zx} \\ \tau_{zy} \\ \tau_{zz} \\ Q_z \end{Bmatrix}$$

$$Q_x = u\boldsymbol{\tau}_{xx} + v\boldsymbol{\tau}_{xy} + w\boldsymbol{\tau}_{xz} - \hat{\boldsymbol{q}}_x$$

$$Q_y = u\boldsymbol{\tau}_{yx} + v\boldsymbol{\tau}_{yy} + w\boldsymbol{\tau}_{yz} - \hat{\boldsymbol{q}}_y$$

$$Q_z = u\boldsymbol{\tau}_{zx} + v\boldsymbol{\tau}_{zy} + w\boldsymbol{\tau}_{zz} - \hat{\boldsymbol{q}}_z$$

where ρ is the fluid density; u, v, and w are the Cartesian velocity components; e is the total internal energy per unit volume, and x, y, and z are the Cartesian coordinates. Variables $\boldsymbol{E}$, $\boldsymbol{F}$, and $\boldsymbol{G}$ are the inviscid flux vectors, $\boldsymbol{E}_v$, $\boldsymbol{F}_v$, and $\boldsymbol{G}_v$ are the viscous flux vectors, $\hat{\boldsymbol{q}}_x$, $\hat{\boldsymbol{q}}_y$, and $\hat{\boldsymbol{q}}_z$ are heat fluxes, and $\boldsymbol{\tau}_{xx}$, $\boldsymbol{\tau}_{xy}$, $\boldsymbol{\tau}_{zy}$, etc., are the stress vectors. A modified two-equation k–ε turbulence model is used for closure.[24]

The Navier–Stokes equations in Eq. (1) are transformed and recast in a generalized body-fitted coordinate system to simplify the treatment of arbitrary geometries. The transformed equations are solved using an implicit finite volume upwind scheme. Flux vector splitting is used to evaluate the flux Jacobians on the left-hand side. The right-hand side fluxes are discretized using a high-order total variation diminishing scheme based on Roe's flux difference splitting. Newton subiterations are used at each time step to find an approximate solution to the nonlinear finite volume discretization. Symmetric Gauss–Seidel relaxation is applied to solve the resulting linear system.

Aerodynamic Damping Calculation

Aerodynamic damping is obtained by calculating the energy exchange between the vibrating blade and the surrounding fluid. The aerodynamic work on the blade is calculated by first obtaining the steady aerodynamic solution for a given operating condition. The blades are then forced into a prescribed harmonic motion (specified mode, frequency, and IBPA) to calculate the unsteady aerodynamic response and work-per-cycle of oscillation. The blade motion is simulated using a dynamic grid deformation technique. For harmonic motion in a selected normal mode, the displacement of any point on the blade $\boldsymbol{X}(x, y, z, t)$ can be written in terms of the generalized coordinate $\boldsymbol{q}(t)$ and the modal deflection $\boldsymbol{\delta}(x, y, z)$ as

$$\boldsymbol{X}(x, y, z, t) = \boldsymbol{q}(t)\boldsymbol{\delta}(x, y, z) \tag{2}$$

The work-per-cycle can then be calculated as

$$W = \int_0^T \int_{\text{surface}} p \, \mathrm{d}\boldsymbol{A} \cdot \left(\frac{\partial \boldsymbol{X}}{\partial t} \right) \mathrm{d}t \tag{3}$$

where T is the time period of oscillation, p is the blade surface pressure, and $\boldsymbol{A}$ is the surface area vector. For a harmonic motion prescribed as

$$\boldsymbol{q}(t) = \boldsymbol{q}_0 \sin(\omega t + \phi) \tag{4}$$

with amplitude of motion $\boldsymbol{q}_0$, vibration frequency ω, and IBPA ϕ, the work-per-cycle of oscillation, using Eqs. (2–4), can be rewritten as

$$W = \int_0^T \int_{\text{surface}} p \, \mathrm{d}\boldsymbol{A} \cdot \boldsymbol{\delta}\boldsymbol{q}_0 \omega \cos(\omega t + \phi) \, \mathrm{d}t \tag{5}$$

The aerodynamic damping associated with the blade motion is calculated by taking the ratio of work and the associated kinetic energy of the blade over one cycle of oscillation[25]

$$W/K_E = -\left(8\pi\gamma/\sqrt{1-\gamma^2}\right) \tag{6}$$

where γ the damping ratio and K_E the average kinetic energy over one cycle of oscillation of the blade are defined as

$$\gamma = \frac{C}{C_{\text{cr}}} \tag{7}$$

$$C_{\text{cr}} = 2m\omega \tag{8}$$

$$K_E = \frac{1}{T} \int_0^T \int_{\text{surface}} \frac{1}{2} m \dot{X}^2 \, \mathrm{d}A \, \mathrm{d}t \tag{9}$$

where C is the damping, C_{cr} is the critical damping, m is mass per unit area of the blade, and $\dot{X}$ is the velocity at any point on the blade surface due to vibration.

For small values of γ,

$$\sqrt{1-\gamma^2} \approx 1 \tag{10}$$

When Eqs. (10) and (6) are combined, the damping ratio can be calculated as

$$\gamma = -(W/8\pi K_E) \tag{11}$$

Negative aerodynamic damping implies flutter instability. Phase-lagged boundary conditions based on the direct store method are used to calculate the nonzero IBPA oscillations, which eliminates the need to model multiple blade passages.

Results and Discussion

A 22-in.-scale (0.5588 m) model of an experimental transonic fan with 22 blades (Fig. 1) was tested in a rig. The design operating condition for the model tested consisted of a mass flow of 44.85 kg/s with a relative tip Mach number of 1.4. The fan fluttered at several part speed conditions in the first natural mode for the two nodal diameter forward traveling wave[15] between the operating line and predicted stall line. The first mode shape of the blade (natural frequency 351 Hz) at design operating speed is shown in Fig. 2. The contours represent the total modal displacement. The mode shows a high degree of twist–bend coupling in the outboard region.

Calculated fan rotor performance for the 90% speed is compared with experimentally measured performance data in Fig. 3. Good comparison is seen for the speed line with small differences near the choke condition. The variation of aerodynamic damping at 90% speed for 32.73-deg IBPA (two nodal diameter forward traveling wave) is shown in Fig. 4. From the choke condition as the back pressure is increased, which results in a reduction in the mass flow and the operating point moving toward peak efficiency, a small increase in aerodynamic damping is seen as the flowfields become more organized. Increasing the back pressure further, thus moving the operating condition toward stall, results in a rapid decrease in the aerodynamic damping. For the given operating condition, a negative aerodynamic damping could not be obtained by further decreasing the mass flow due to numerical problems. Steady flow for mass flows lower than shown on Fig. 3 (mass flow 36 kg/s) could not be calculated because of numerical instability as a result of shock-induced flow separation. However, it is evident from Fig. 4 that

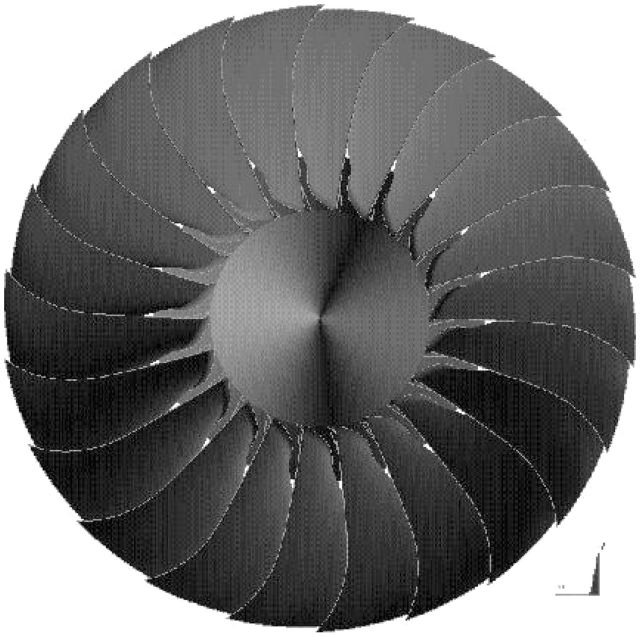

Fig. 1 Transonic fan.

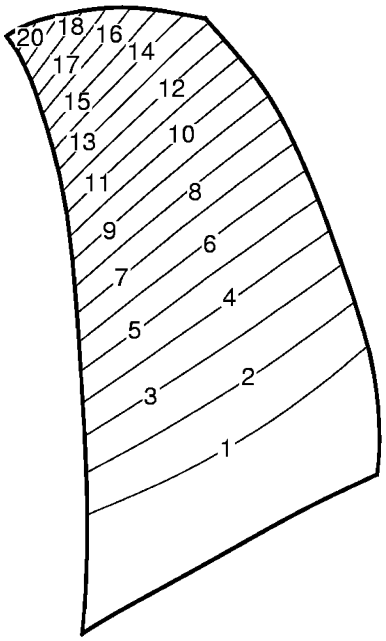

Fig. 2 First natural mode: for level 20, total deformation is 3.70; for level 19, 3.51; for level 18, 3.33; for level 17, 3.15; for level 16, 2.97; for level 15, 2.79; for level 14, 2.61; for level 13, 2.43; for level 12, 2.25; for level 11, 2.07; for level 10, 1.89; for level 9, 1.71; for level 8, 1.52; for level 7, 1.34; for level 6, 1.16; for level 5, 0.98; for level 4, 0.80; for level 3, 0.62; for level 2, 0.44; and for level 1, 0.26.

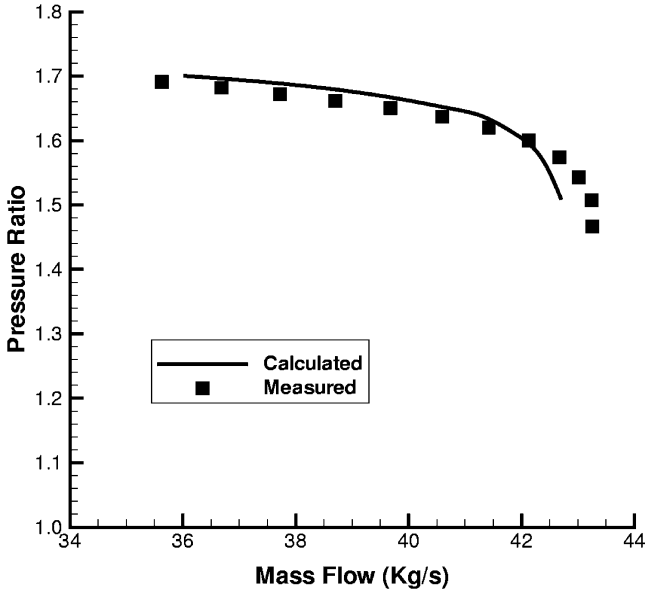

Fig. 3 Comparison of performance for a forward swept fan at 90% rotational speed.

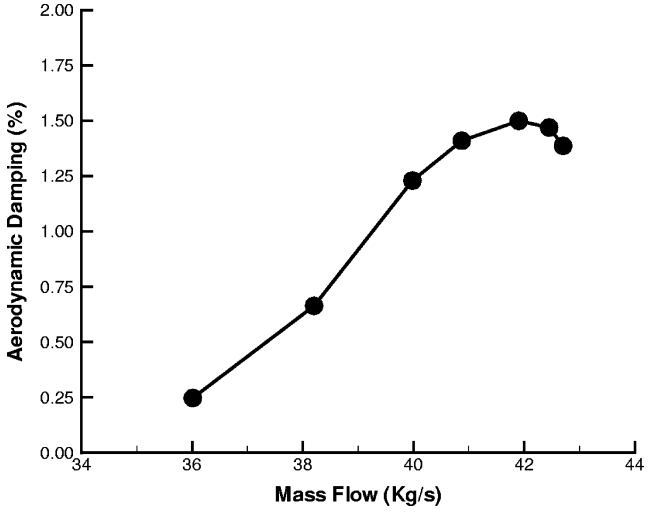

Fig. 4 Aerodynamic damping variation with mass flow for 32.73-deg IBPA.

flutter instability will occur with a further increase in back pressure for this flow condition. All subsequent results presented here are for the 90% rotational speed at the mass flow of 36 kg/s.

Figure 5 shows the steady flow Mach number variation just outside the boundary layer over the suction and pressure surfaces for the lowest calculated mass flow condition. Shock wave structures are evident from Figs. 5. A shock wave appears on the suction surface over the entire span. The shock is near the leading edge on the inboard sections and moves downstream on the blade surface in the outboard region, appearing just aft of midchord near the blade tip. On the pressure surface, the shock impinges in the outboard regions near the blade leading edge. This shock wave pattern is typical of a flow condition referred to as moderate-to-high loading on blades with a supersonic leading edge operating in subsonic axial flow. As the back pressure is increased, thus, moving the operation point toward the stall line, the shock waves become stronger, resulting in flow separation on the suction surface in the middle section of the blade. The separation is large enough to stall the blade, resulting in a breakdown of the numerical analysis. The observed breakdown of the analysis due to flow separation could not be verified because velocity profiles in the blade passage were not measured during the experiment.

Figure 6 shows the work distribution on the blade surface for 32.73-deg IBPA. It can be seen that the contribution toward blade stability is limited primarily to outboard stations on the blade and the majority of the blade does not measurably contribute toward blade stability characteristics. The suction surface shows an area of positive work concentrated near the midchord in the outboard regions, whereas the pressure surface shows a small area of negative work on the blade near the tip leading edge. When compared with Mach contours shown in Fig. 5, it is clear that the area of energy exchange on the blade surface is located in the vicinity of the shock. However, despite the shock extending almost over the entire blade span on the suction surface, only the outboard regions contribute toward the energy exchange. Note that in the present formulation

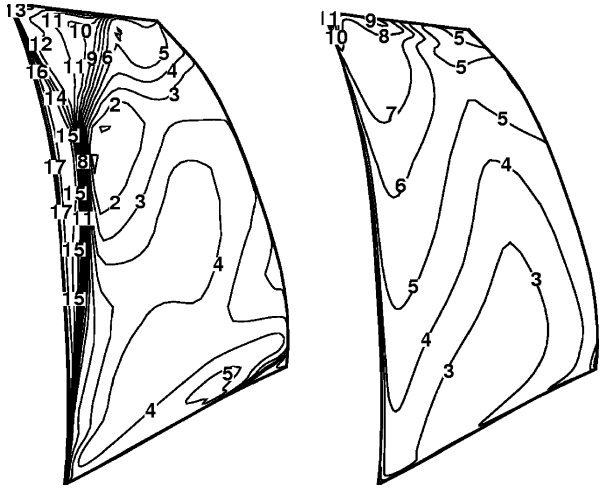

a) Suction b) Pressure

Fig. 5 Mach contours near blade surfaces: for level 18, Mach = 1.8; for level 17, Mach = 1.7; for level 16, Mach = 1.6; for level 15, Mach = 1.5; for level 14, Mach = 1.4; for level 13, Mach = 1.3; for level 12, Mach = 1.2; for level 11, Mach = 1.1; for level 10, Mach = 1.0; for level 9, Mach = 0.9; for level 8, Mach = 0.8; for level 7, Mach = 0.7; for level 6, Mach = 0.6; for level 5, Mach = 0.5; for level 4, Mach = 0.4; for level 3, Mach = 0.3; for level 2, Mach = 0.2; and for level 1, Mach = 0.1.

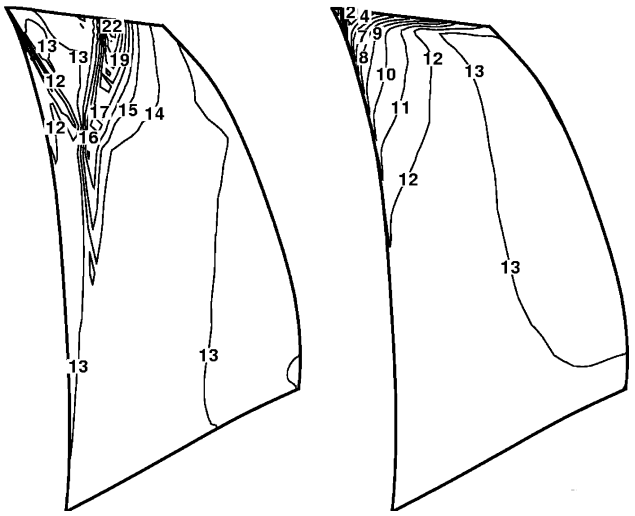

a) Suction b) Pressure

Fig. 6 Work distribution on blade surface for 32.73-deg IBPA: for level 25, work = 0.0060; for level 24, work = 0.0055; for level 23, work = 0.0050; for level 22, work = 0.0045; for level 21, work = 0.0040; for level 20, work = 0.0035; for level 19, work = 0.0030; for level 18, work = 0.0025; for level 17, work = 0.0020; for level 16, work = 0.0015; for level 15, work = 0.0010; for level 14, work = 0.0005; for level 13, work = 0.0000; for level 12, work = −0.0005; for level 11, work = −0.0010; for level 10, work = −0.0015; for level 9, work = −0.0020; for level 8, work = −0.0025; for level 7, work = −0.0030; for level 6, work = −0.0035; for level 5, work = −0.0040; for level 4, work = −0.0045; for level 3, work = −0.0050; for level 2, work = −0.0055; and for level 1, work = −0.0060.

positive work on the blade is destabilizing, whereas negative work is stabilizing.

A more quantitative relation between shock location and work contribution is shown in Fig. 7. Figure 7 shows the steady pressure distribution and associated work distribution at the 95% span location of the blade. The vertical axis on the left of Fig. 7 shows the pressure coefficient on the blade surface, whereas the vertical axis on the right shows the local work distribution on the blade surface. The suction surface shock located just aft of the midchord is seen

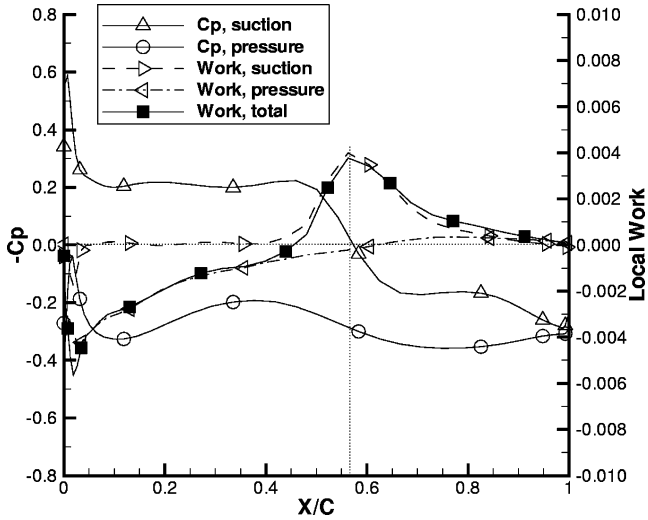

Fig. 7 Variation of pressure coefficient and local work at 95% span for 32.73-deg IBPA.

to contribute positive work in its vicinity with very little contribution from other areas of the blade. On the pressure surface, the shock is located near the leading edge and contributes to the negative work on the surface. It can be clearly seen that the stabilizing and destabilizing work is strongly associated with the shock wave location.

Figures 6 and 7 also help explain the observed decrease in stability with increasing back pressure as shown in Fig. 4. As the back pressure is increased, the mass flow through the rotor decreases, causing the incidence angle on the blade to increase. This results in the shock structure moving upstream on the blade with pressure surface shock moving completely off the blade surface leading to an unstarted flow condition. As the pressure surface shock moves off the blade surface, the associated stabilizing effect of the shock is also lost and the stability characteristics are then dominated by the suction surface work contribution, which is largely destabilizing. This results in decreased blade stability, eventually leading to flutter.

The presence of the shock on the suction surface and its positive work contribution is the primary reason for the aerodynamic damping variation characteristics seen in Fig. 4 for the 32.73-deg IBPA. However, the suction surface shock does not always produce a destabilizing effect. Figure 8 shows the work distribution on the suction surface, and Fig. 9 shows the chordwise variation of work at 95% span near stall condition for six different IBPAs. The suction surface shock is seen to induce a stabilizing effect for several IBPAs. This is because the work done on the blade depends not only on the shock impulse, but also on the phase relation between the shock motion and the blade motion. As the IBPA is changed, it alters the phase between the shock motion and the blade motion. Therefore, knowledge of shock location and shock strength alone is not sufficient to determine the work contribution from the shock. The phase relation between shock motion and blade motion is also needed. This phase relation will depend on the operating condition, IBPA, and frequency of vibration.

Some preliminary calculations have shown the phase between shock motion and work contribution to be harmonically dependent on IBPA. Figure 10 shows the variation of aerodynamic damping with IBPA for 36-kg/s mass flow. A sinusoidal curve of the form $a_0 + a_1 \sin(\phi + \psi)$ was fit to the calculated aerodynamic damping values. Here a_0, a_1, and ψ are constants that are determined by curve fitting the calculated aerodynamic damping, and ϕ is the IBPA. The harmonic curve fit is also shown on Fig. 10. The variation of damping is seen to match reasonably well with the curve fit, indicating that the aerodynamic damping varies sinusoidally with IBPA for a sinusoidal blade motion.

Presence of shock waves can introduce highly nonlinear effects in the flowfield. However, for small-amplitude blade motion, where a shock is present throughout the vibration cycle and remains on

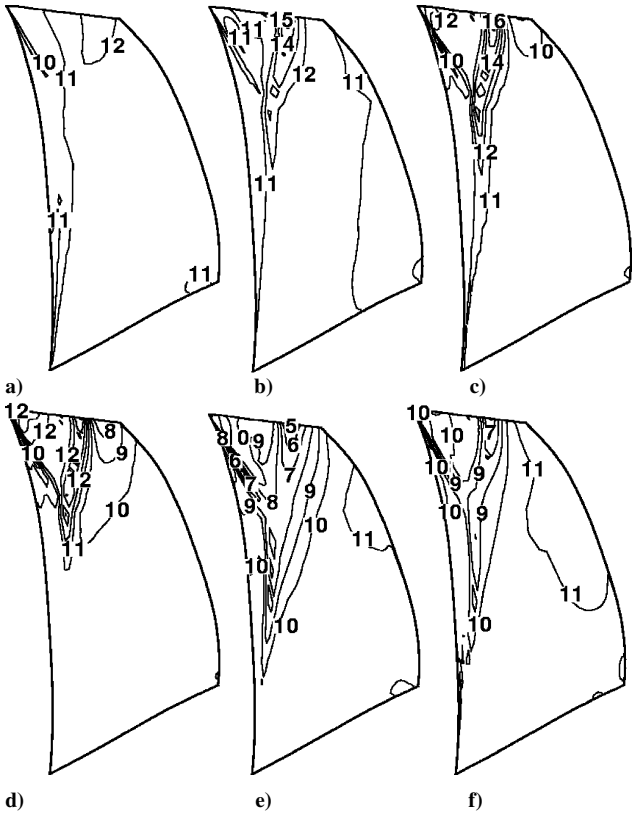

Fig. 8 Work distribution on the suction surface for different IBPAs; for level 21, work = 0.010; for level 20, work = 0.009; for level 19, work = 0.008; for level 18, work = 0.007; for level 17, work = 0.006; for level 16, work = 0.005; for level 15, work = 0.004; for level 14, work = 0.003; for level 13, work = 0.002; for level 12, work = 0.001; for level 11, work = 0.000; for level 10, work = −0.001; for level 9, work = −0.002; for level 8, work = −0.003; for level 7, work = −0.004; for level 6, work = −0.005; for level 5, work = −0.006; for level 4, work = −0.007; for level 3, work = −0.008; for level 2, work = −0.009; and for level 1, work = −0.010: a) 0 deg, b) 32.73 deg, c) 65.45 deg, d) 98.18 deg, e) 180 deg, and f) −98.18 deg.

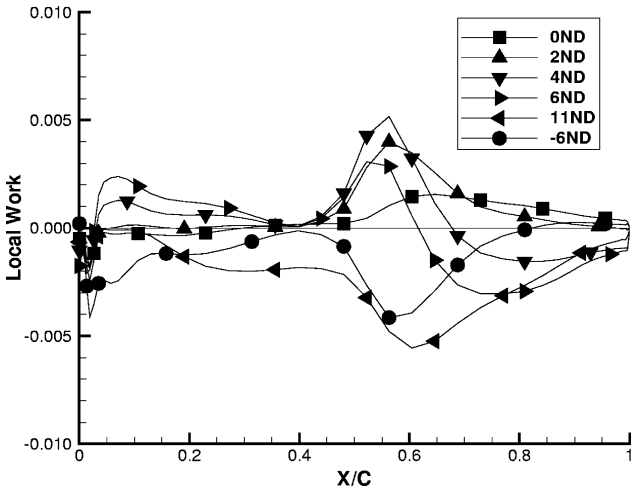

Fig. 9 Variation of work along the chord with IBPA for 95% span.

the blade surface, the influence of the shock wave motion can be considered linear. Figure 11 shows the real and imaginary components of the unsteady pressure at 95% span for 32.73-deg IBPA on the suction surface for the first and second harmonics. The second harmonic is seen to be an order of magnitude smaller than the first harmonic, indicating that the nonlinearities induced by shock motion are small and the flowfield can be considered to be linear for the amplitudes of vibration used in the present analysis. Lindquist

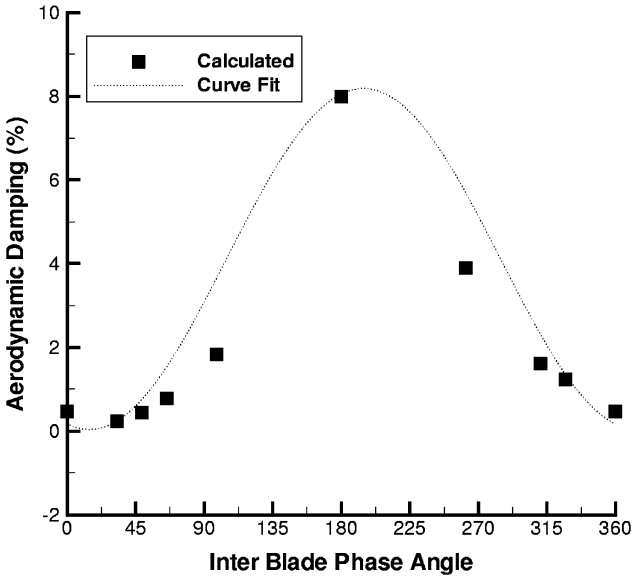

Fig. 10 Variation of aerodynamic damping with IBPA near stall condition.

and Giles[26] have also shown similar linear behavior of the flowfield because of shock motion.

Based on the observations from this study, a basic algebraic model can be constructed to better understand the influence of shock wave on blade stability. When the shock is assumed to be a discontinuity in pressure and the motion of shock is assumed to be harmonic for a harmonic blade motion, the model shown in Fig. 12 can be constructed. When the blade is assumed to be undergoing a small amplitude pitching motion, the work done on the blade surface due to the shock can be calculated from Eq. (5) to be

$$W_S = -A(\bar{\alpha}, \bar{a}, \Delta p_S, d)\sin(\phi + \beta) \tag{12}$$

$$W_P = B(\bar{\alpha}, \bar{b}, \Delta p_P, f)\sin(\phi + \lambda) \tag{13}$$

where

$$A = \bar{\alpha}\bar{a}\pi d(p_2 - p_1) \tag{14}$$

$$B = \bar{\alpha}\bar{b}\pi f(p_4 - p_3) \tag{15}$$

where W_S is the suction surface work, W_P is the pressure surface work, $\bar{\alpha}$ is the amplitude of blade motion, $\bar{a}$ and $\bar{b}$ are amplitudes of the shock motion, Δp_S and Δp_P are the pressure differences across the shock, d and f are the distances between the elastic axis and the location of the shock wave, and β and λ are the phase differences between the shock motion and the blade motion on suction and pressure surfaces, respectively, and ϕ is the IBPA.

Equations (12) and (13) provide an algebraic expression for estimating the work done by a shock on the two blade surfaces. Although in the present form Eqs. (12) and (13) cannot be used quantitatively, they can be used to determine some basic characteristics of the influence of shock on stability. For a pitching motion, on the suction surface, A will be positive if the shock is downstream of the elastic axis ($d > 0$), and A will be negative if the shock is upstream of the elastic axis ($d < 0$). Therefore, the work W_S will be positive for positive A and $\phi + \beta$ between π and 2π, or negative A and $\phi + \beta$ between 0 and π. The value of $\phi + \beta$ will depend on the operating condition, vibration mode, and the IBPA. Therefore, for any given operating point and mode shape, the shock will provide a stabilizing effect for some IBPAs and a destabilizing effect for other IBPAs. This behavior is evident from Figs. 8 and 9. For the given configuration, the shock is downstream of the elastic axis. Note that although the work on suction and pressure surfaces has opposite signs in Eqs. (12) and (13), the motion of shock on the two surfaces will be

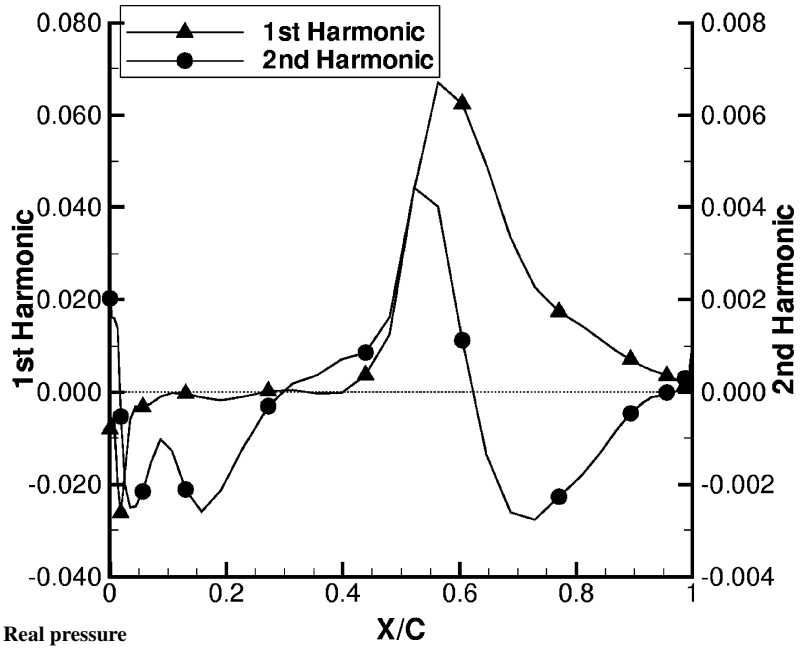

a) Real pressure

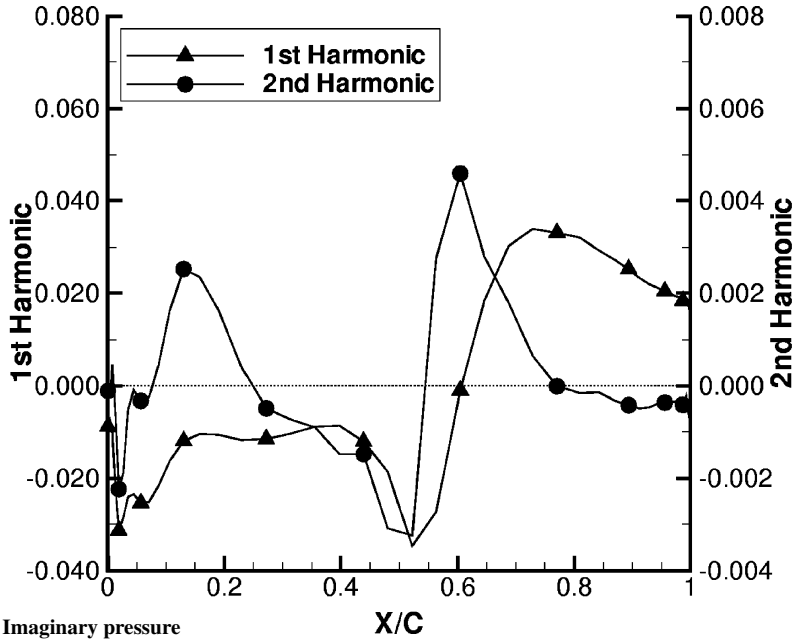

b) Imaginary pressure

Fig. 11 Variation of real and imaginary components of the unsteady pressure at 95% span for 32.73-deg IBPA.

approximately 180 deg out of phase, and thus, in general, the relation between the shock location and the sign of work contribution will be the same for both surfaces.

Equations (12) and (13) indicate the amplitude of work contribution from the shock to have a linear dependence on the location of the torsion axis. This dependence can be easily understood because the work done on the blade surface is equal to the product of pressure impulse and the displacement of the blade surface in the direction normal to the surface at which the pressure is acting. For a pure pitching motion, the amplitude of displacement of blade surface varies linearly with the distance from the pitching axis. Therefore, for a given value of pressure jump across the shock, the work done by the shock will be linearly dependent on the distance of the shock from elastic axis and the work contribution will switch sign by moving the shock from one side of the elastic axis to the other. Furthermore, noting the variation in Fig. 10 and realizing that for a compressible flow the time variation of the aerodynamic loading of blade will have a phase difference with blade motion, one can see the harmonic dependence of work on the phase between blade motion and aerodynamic loading.

Equations (12) and (13) have been derived here for a pure pitching motion. Note that a pure bending motion is a special case of pitching motion. For a pitching axis tending to $-\infty$ and a pitching motion with infinitesimal amplitude $\bar{\alpha}$ such that

$$\underset{\to\infty}{d} \times \underset{\to 0}{\bar{\alpha}} = h \tag{16}$$

where h is a finite quantity representing amplitude of plunging motion positive downward, Eqs. (12) and (13) will describe the work due to a plunging motion.

Results shown in Fig. 10 suggest that the IBPA ϕ and the phase between shock motion and blade motion (β and λ) can be considered loosely coupled. If this can be shown more rigorously, then β and λ can be obtained for a given operating condition from Eqs. (12) and

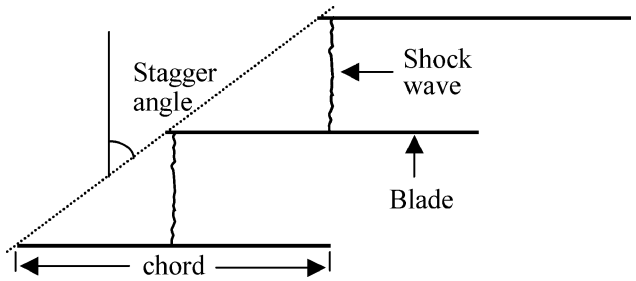

a) Typical shock structure for turbomachinery blade row

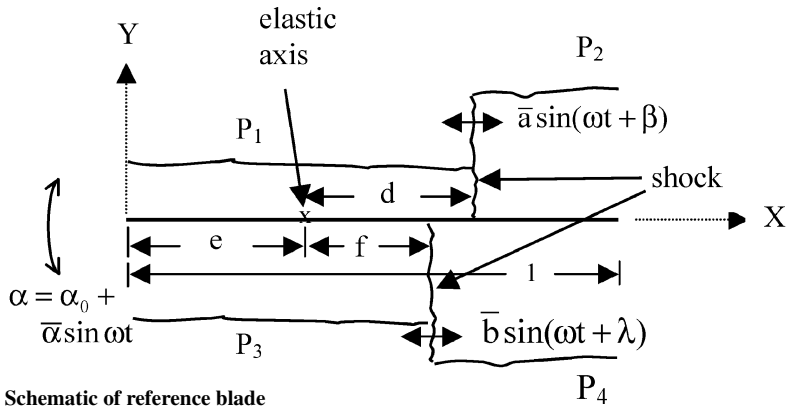

b) Schematic of reference blade

Fig. 12 Model for an oscillating blade.

(13) by analyzing the blade row for 0 IBPA. Alternatively, a model for β and λ can be developed based on observations from other flutter analyses performed on simple geometries. Because work is a scalar quantity, work contribution from all of the shock waves and blade motions can be added to obtain the overall stability of the system. Note, however, that although the largest work contribution on a blade surface comes from a shock, other areas of the blade could also contribute to the energy exchange.

Summary

A study of the influence of a normal shock on flutter instability has been made in the present effort. The study showed that the shock has both a stabilizing and a destabilizing effect on blade stability. The effect of the shock wave on stability is contained primarily in the outboard region of the blade and depends on the shock location and interblade phase angle. The study also showed that the shock motion, as long as it is small, induces very little nonlinearity; thus, a linearized method can be successfully used to predict the flutter observed for the fan analyzed. The interblade phase angle was found to have a significant impact on blade stability with smaller IBPAs manifesting instability. A simple model was developed that showed that the location of the shock wave with respect to the elastic axis and phase relationship of shock motion with respect to blade motion were the main factors determining the impact of shock wave on blade stability. The model helped explain the observed flutter characteristics and showed the relationship between stability characteristics and various parameters.

Acknowledgments

This work was carried out under Contract NAS 3-01116 for the Quiet Aircraft Technology Project from NASA John H. Glenn Research Center at Lewis Field, Cleveland, Ohio. J. B. Min was the Contract Monitor.

References

[1]Lane, F., and Friedman, M., "Theoretical Investigation of Subsonic Oscillating Blade-Row Aerodynamics," NACA TN 4136, Feb. 1958.

[2]Smith, S. N., "Discrete Frequency Sound Generation in Axial Flow Turbomachines," Rept. R & M 3709, British Aeronautical Research Council, London, March 1972.

[3]Verdon, J. M., "Unsteady Aerodynamic Methods for Turbomachinery Aeroelastic and Aeroacoustic Applications," *AIAA Journal*, Vol. 31, No. 2, 1993, pp. 235–250.

[4]He, L., "An Euler Solution for Unsteady Flows Around Oscillating Blades," *Journal of Turbomachinery*, Vol. 112, No. 4, 1989, pp. 714–722.

[5]Gerolymos, G. A., and Vallet, I., "Validation of 3-D Euler Methods for Vibrating Cascade Aerodynamics," American Society of Mechanical Engineer, ASME Paper 94-GT-294, June 1994.

[6]Bakhle, M. A., Srivastava, R., Keith, T. G., Jr., and Stefko, G. L., "A 3D Euler/Navier–Stokes Aeroelastic Code for Propulsion Applications," AIAA Paper 97-2749, July 1997.

[7]Clark, W. S., and Hall, K. C., "A Time-Linearized Navier–Stokes Analysis of Stall Flutter," *Journal of Turbomachinery*, Vol. 122, No. 3, 2000, pp. 467–476.

[8]Giles, M., and Haimes, R., "Validation of a Numerical Method for Unsteady Flow Calculations," *Journal of Turbomachinery*, Vol. 115, No. 1, Jan. 1993, pp. 110–117.

[9]Siden, L. D. G., "Numerical Simulation of Unsteady Viscous Compressible Flows Applied to a Blade Flutter Analysis," American Society of Mechanical Engineers, ASME Paper 91-GT-203, June 1991.

[10]He, L., and Denton, J. D., "Three Dimensional Time Marching Inviscid and Viscous Solutions for Unsteady Flows Around Vibrating Blades," *Journal of Turbomachinery*, Vol. 116, No. 3, July 1994, pp. 469–476.

[11]Williams, M. H., Cho, J., and Dalton, W. N., "Unsteady Aerodynamic Analysis of Ducted Fans," *Journal of Propulsion and Power*, Vol. 7, No. 5, 1991, pp. 800–804, 1991.

[12]Gerolymos, G. A., "Coupled Three-Dimensional Aeroelastic Stability Analysis of Bladed Disks," *Journal of Turbomachinery*, Vol. 115, No. 4, Oct. 1993, pp. 791–799.

[13]Srivastava, R., and Reddy, T. S. R., "Comparative Study of Coupled-Mode Flutter-Analysis Methods for Fan Configurations," *Journal of Propulsion and Power*, Vol. 15, No. 3, 1999, pp. 447–453.

[14]Panovsky, J., Bakhle, M. A., and Srivastava, R., "Flutter Characteristics of a Forward-Swept Fan," *Proceedings of the 7th National Turbine Engine High Cycle Fatigue Conference*, Universal Technology Corp., Dayton, OH, April 2002.

[15]Srivastava, R., Bakhle, M. A., and Keith, T. G., Jr., "Numerical Simulation of Aerodynamic Damping for Flutter Analysis of Turbomachinery Blade Rows," *Journal of Propulsion and Power*, Vol. 19, No. 2, 2003, pp. 260–267.

[16]Sanders, A. J., Hassan, K. K., and Rabe, D. C., "Experimental and Numerical Study of Stall Flutter in a Transonic Low-Aspect Ratio Fan Blisk," *Journal of Turbomachinery*, Vol. 126, No. 1, Jan. 2004, pp. 166–174.

[17]Shibata, T., and Kaji, S., "Role of Shock Structures in Transonic Fan Rotor Flutter," *Proceedings of the 8th International Symposium of Unsteady Aerodynamics and Aeroelasticity of Turbomachines*, Kluwer, Dordrecht, The Netherlands, 1997, pp. 733–747.

[18]Isomura, K., and Giles, M. B., "A Numerical Study of Flutter in a Transonic Fan," *Journal of Turbomachinery*, Vol. 120, No. 3, 1998, pp. 500–507.

[19]Fite, B. E., "Aerodynamic Overview of the NASA/Honeywell Quiet High Speed Fan Test," *Noise Reduction/Quiet Aircraft Technology Technical Working Group Meeting*, NASA Langley Research Center, Langley, VA, April 2001.

[20]Janus, J. M., "Advanced 3-D CFD Algorithm for Turbomachinery," Ph.D. Dissertation, Mississippi State Univ., Mississippi State, MS, May 1989.

[21]Chen, J. P., "Unsteady Three-Dimensional Thin-Layer Navier–Stokes Solutions for Turbomachinery in Transonic Flow," Ph.D. Dissertation, Mississippi State Univ., Mississippi State, MS, Dec. 1991.

[22]Chen, J. P., and Barter, J., "Comparison of Time-Accurate Calculations for the Unsteady Interaction in Turbomachinery Stage," AIAA Paper 98-3292, July 1998.

[23]Barter, J. W., Vitt, P. H., and Chen, J. P., "Interaction Effects in a Transonic Turbine Stage," American Society of Mechanical Engineers, ASME Paper 2000-GT-0376, May 2000.

[24]Shih, T.-H., Liou, W. W., Shabbir, A., Yang, Z., and Zhu, J., "A New k–ε Eddy Viscosity Model for High Reynolds Number Turbulent Flows," *International Journal of Computers and Fluids*, Vol. 24, No. 3, 1995, pp. 227–238.

[25]Carta, F. O., "Coupled Blade-Disk-Shroud Flutter Instabilities in Turbojet Engine Rotors," *Journal of Engineering for Power*, Vol. 89, No. 3, July 1967, pp. 419–426.

[26]Lindquist, D. R., and Giles, M. B., "Validity of Linearized Unsteady Euler Equations with Shock Capturing," *AIAA Journal*, Vol. 32, No. 1, 1994, pp. 46–53.